Picosecond Time-Resolved Measurements of Dense Plasma Line Shifts

Understanding the time-averaged and time-dependent response of ions in dense plasma is important for correctly interpreting and modeling atomic structure and radiation transport in extreme environments,[1,2] including stellar atmospheres[3] and imploding inertial fusion capsules.[4] The potential in and near an ion immersed in a dense plasma is influenced by its bound electrons, free electrons, and neighboring ions. These influences can change the radiative and thermodynamic properties of the plasma by modifying the energy levels that are available to an ion and causing energy-level shifts.[5]

Dense plasma line shifts originate from free-electron modification of the ionic potential.[1,2] Free electrons in the ion sphere screen the nuclear charge and shift bound energy levels toward the continuum. The energy separation between levels is decreased for a given bound-electron configuration, and emission lines are shifted to lower photon energies. Correct identification of this effect helped resolve the disparity between spectroscopically inferred white dwarf masses and the results from other measurement methods and the predictions of general relativity.[6]

While dense plasma line shifts have been described mathematically[7] and confirmed experimentally,[8] few measurements have tested line-shift model predictions at high energy density, leading to an incomplete picture of how this process is understood and modeled in extreme conditions. Data comparisons to line-shift model predictions in this regime have been hampered by the difficulty of obtaining uniform, well-characterized, and high-energy-density (HED) plasmas. Line-shift measurements are especially needed in hot dense plasmas to provide a stringent test for analytic and detailed atomic kinetics and radiative-transfer calculations. Equally important, line-shift measurements can provide a sensitive benchmark for free-electron distribution models within the ion sphere—an important application of the N-body problem.[9]

This article reports the first picosecond time-resolved measurements of dense plasma line shifts of the $1s2p$–$1s^2$ transition in He-like Al ions as a function of the instantaneous plasma conditions. Line shifts were measured with picosecond time resolution for free-electron densities of 1 to 5×10^{23} cm^{-3} and temperatures of 250 to 375 eV. The plasma conditions were inferred with well-quantified errors from spectroscopic measurements of the Al He$_\alpha$ complex. The data are compared to a generalized analytic model proposed by Li et al.[10] based on a parameterization of numerical ion-sphere model calculations. The predicted line shifts show broad agreement with the data over the full range of densities and temperatures studied, with evidence for deviation from the experimental data at the most-extreme densities. This work provides an experimental test of a simplified method that calculates quantum-number–dependent energy level shifts for ions in dense, finite-temperature plasma.

The experiments were carried out at LLE's Multi-Terawatt (MTW) Laser Facility.[11] Figure 150.23(a) shows the experimental setup. The laser directly irradiated small-mass targets with 0.7-ps, ≤16-J pulses at the laser's fundamental wavelength (λ = 1054 nm) or second harmonic. The laser was focused to an ~5-μm full-width-at-half-maximum (FWHM) focal spot by an f/3 off-axis parabolic mirror at normal incidence to the target at intensities greater than 10^{18} W/cm^2. The targets were thin plastic foils with a buried Al microdot. The microdot was vacuum deposited in a 0.2-μm layer on a 1-μm parylene-N (CH) support. The thickness of the front parylene-N overcoat was varied between 0 and 2 μm to access different plasma densities. The Al microdot was kept purposefully thin to limit spatial gradients, while the outer plastic layers constrain sample expansion to achieve near-solid-density conditions.[12]

High-intensity laser pulses with low contrast reduce the maximum electron density that can be achieved in buried-layer target interactions by causing the target to prematurely heat and decompress.[13] In the experiments reported here, free-electron densities of up to 2×10^{23} cm^{-3} were achieved at the laser's fundamental wavelength with a measured temporal contrast of the order of 10^8 up to 100 ps prior to the main pulse.[14] Experiments with high-contrast, frequency-doubled pulses achieved free-electron densities of the order of 5×10^{23} cm^{-3}. Based on work by previous authors and the measured contrast of the 1ω
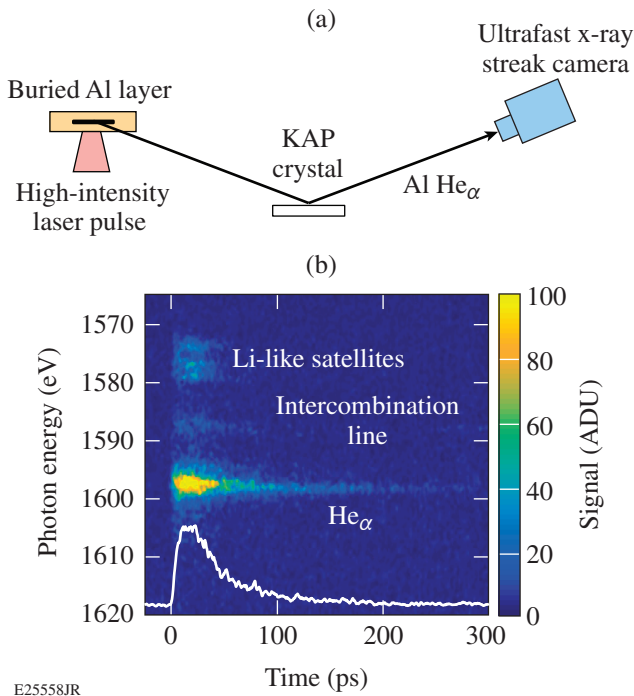
Figure 150.23

(a) Experimental setup. (b) Example streaked He$_\alpha$ emission from a rapidly heated Al surface layer. The Li-like satellites, intercombination line, and He$_\alpha$ line are shown. KAP: potassium acid phthalate; ADU: analog digital unit.

beam, the temporal contrast of the frequency-doubled beam is estimated to be 10^{12} (Ref. 15); however, no on-shot contrast measurement was available for this particular experiment. Residual 1ω light was rejected at a spectral contrast of the order of 10^{12} by six transport mirrors with 99% 1ω extinction coatings.

Picosecond streaked x-ray spectroscopy was used to infer the density and temperature of the Al layer. For this measurement, a conically curved potassium acid phthalate (KAP) streaked x-ray spectrometer was used in combination with a time-integrating flat pentaerythritol (PET) crystal spectrometer. The streaked spectrometer was configured to study Al He$_\alpha$ ($1s2p$–$1s^2$) thermal line emission with spectral resolving power $E/\Delta E \sim 1000$ and 2-ps temporal resolution.[16] Time-integrated spectra were measured on each shot and used to correct the streaked spectra for variations in spectral sensitivity introduced by the photocathode.[17]

It is noted that the plasma-induced line shifts measured in the experiment could be exaggerated or disguised by streak camera charge-coupled–device (CCD) clocking errors. The CCD clocking was measured offline using a structured photocathode illuminated by a static x-ray source. The tests identified

a 0.46±0.01° correction that was applied to the experimental data. Experimental tests with low-density, laser-driven Al plasmas confirm that the clocking offset was properly corrected.

Figure 150.23(b) shows example streaked data where the dispersion of the streaked x-ray spectrometer was determined *in situ* from the emission lines of He- and Li-like Al ions at low plasma density. A well-resolved emission spectrum was selected after the plasma was allowed to expand for 12 ps after the high-intensity pulse [Fig. 150.24(a)]. The initial He$_\alpha$ and intercombination line positions cannot be directly identified with tabulated transition energies because the plasma environment modifies the ionic energy-level structure. The Li-like satellite lines are not expected to shift measurably because of the screening effect of the $n = 2$ spectator electron.[18] The
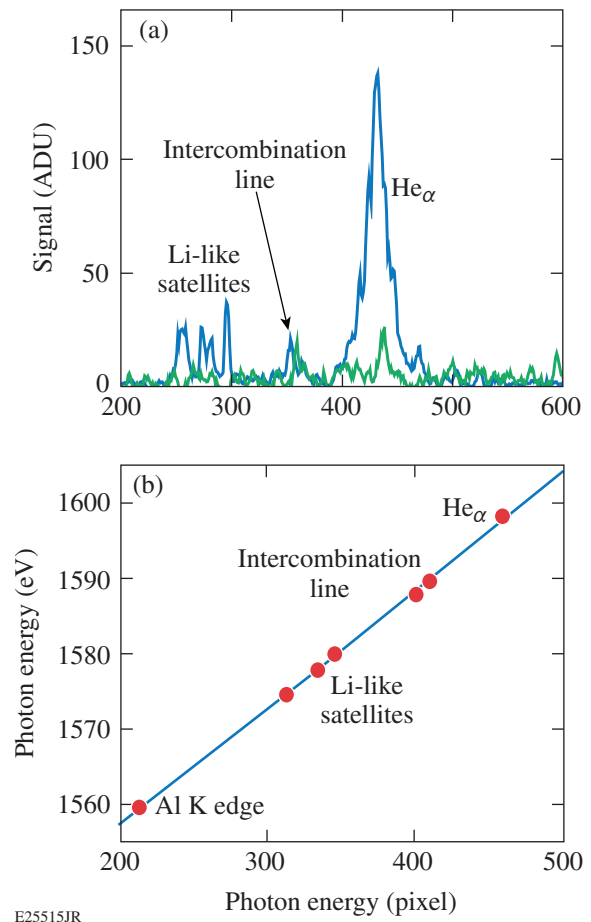

Figure 150.24

(a) X-ray spectra from an Al surface layer at $t_0 + 12$ ps (blue) and $t_0 + 275$ ps (green). (b) The measured peak positions were identified with tabulated transition energies using an analytic dispersion calibration derived from Bragg's law for the spectrometer geometry.

green trace in Fig. 150.24(a) corresponds to the latest time in the plasma evolution that could be reliably measured, corresponding to $t_0 + 275$ ps, where t_0 is the arrival time of the high-intensity laser pulse at the target. At this time, the plasma consists of approximately isolated radiators and the He_α resonance and intercombination lines are observed at a higher photon energy. The observed positions of these lines are constant in time and provide an absolute energy fiducial to register the calibration. Additional Al K-edge measurements were carried out to verify the calibration. A 2-μm Al filter placed *in situ* over the detector aperture was backlit by laser-produced x rays and the K-shell absorption edge at 1559.6 eV was recorded. The measured edge location is free from plasma effects and provides an absolute energy fiducial to confirm the dispersion slope and offset.

The measured fiducial position P was related to the photon energy E via Bragg's law for the spectrometer geometry:

$$P\,(\text{pixel}) = A \cdot \tan\left[a\sin\left(\frac{hc}{2d}\frac{1}{E}\right)\right] + B, \quad (1)$$

where A and B are fitting parameters, h is Planck's constant, c is the speed of light, and $2d = 26.64$ Å is the Bragg spacing of the KAP crystal. The results of the calibration are shown in Fig. 150.24(b). A conservative estimate for the uncertainty in peak position yields two pixels, or 0.25 eV. Uncertainty in the location of the K edge is slightly larger because of degraded spectral resolution at the edge of the streak camera field of view, where the K edge was measured. This uncertainty provides the dominant contribution to the calculated error in the measured shifts. The overall uncertainty in the dispersion is within the width of the data points in Fig. 150.24(b). This dispersion was applied to all data collected in this work. An important point for these measurements is that the dispersion was established self-consistently without reference to plasma-dependent fiducials. Previous work[19,20] relied on time-averaged measurements of the K_α line shape to set the dispersion. The technique presented here provides the dispersion over the full spectral range of interest, registered to the cold Al K-shell absorption edge.

Figure 150.25(a) shows the streaked data gathered from an Al layer heated by a 16-J, 0.7-ps pulse focused to $\sim 1 \times 10^{19}$ W/cm^2. The Al was enclosed on both sides by a 1-μm parylene-*N* tamper. The data were corrected for the streak tube's geometric curvature and variations in photocathode spectral sensitivity. The time axis was calibrated in separate tests. The Stark-broadened resonance line and the commensurate strong satellite emission indicate high plasma density over the duration of the experiment. Spectra were averaged over a five-pixel temporal window (shaded region) corresponding to the streak camera's temporal impulse response. A linear background was removed from the data.

The He_α FWHM and He_α-to-satellite intensity ratio was interpreted using a nonlocal-thermodynamic-equilibrium (NLTE) collisional-radiative atomic model[21] to infer the Al density and temperature as a function of time.[2,22] The model calculated synthetic spectra for Al IX–XIV ions over a regular density and temperature grid of 0.1 to 6 g/cm^3 and 100 to 600 eV, respectively. The simulation was carried out in 1-D for a 0.2-μm Al slab. Satellite contributions to the line shape were treated in detail by including transitions from all ions with non-negligible populations. Satellite blending with the
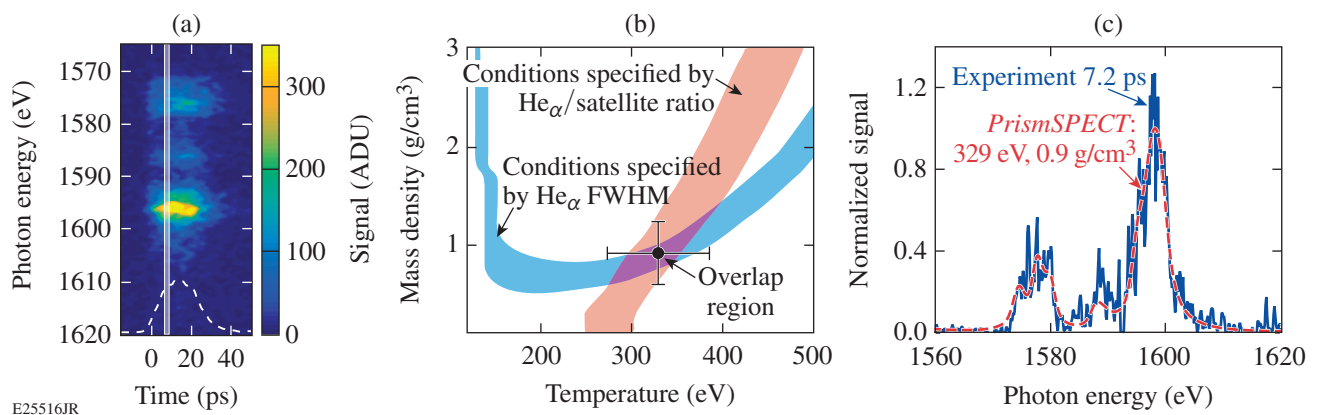

Figure 150.25

(a) Streaked He_α emission from a buried Al layer (1 μm CH). (b) The plasma conditions are inferred from the He_α intensity ratio (red) and full width at half maximum (FWHM) (blue). (c) The synthetic spectrum corresponding to T_e = 330 eV and ρ = 0.9 g/cm^3 (red) is compared to the data (blue).

E25516JR

resonance line may otherwise be misinterpreted as spurious Stark broadening or red shift.[23] The effects of radiation transfer were included using an escape probability approach based on local escape factors to calculate photoexcitation rates.[21] The line profiles were calculated with the effects of Doppler, Stark, natural, Auger, and opacity broadening.[24] The synthetic spectra were convolved with the detector resolving power, and the He_α FWHM and He_α-to-satellite intensity ratio were tabulated for each temperature and density grid point for comparison to the measured spectra. Apparent He_α shifts caused by line broadening and satellite blending were calculated from the model to verify that the observed shifts were caused by true plasma effects.

The experimental He_α-to-satellite intensity ratio was formed over the same spectral bands as the synthetic data. The error was determined from a Monte Carlo study that produced a ratio distribution from uncertainties introduced by photon statistics and the analysis procedure. The distribution variance characterizes the ratio error with coupled sources of uncertainty. For the lineout selected in Fig. 150.25(a), the ratio was 2.5±0.5. Figure 150.25(b) shows the temperature and density contour specified by the measured ratio (red). The He_α FWHM provides a second measurement to constrain the inferred conditions.[25] The FWHM was measured from a spline fit through the data to minimize random error introduced by statistical signal fluctuations. Noise was considered separately as a source of uncertainty by calculating the probability distribution for the measured width based on the likelihood that statistical signal fluctuations could be spuriously detected as FWHM crossing points. For the data shown, the width was 5.3±0.6 eV. The measured FWHM specifies a second contour in temperature and density space (blue) that constrains the inferred temperature and density. The width of the two contours and the size of the overlap region are related to the uncertainties in the measured quantities.

An estimate for the true temperature and density is calculated from the mean temperature and density in the overlap region. The error in the estimated temperature and density corresponds to the extent of the overlap region along each axis. The conditions were inferred to be 330±56 eV and 0.9±0.3 g/cm^3 (n_e = 2.2±0.8 × 10^{23} cm^{-3}). Figure 150.25(c) shows the unfiltered spectrum and the model prediction for the measured conditions. The model considers the instrument resolving power and reproduces the experimental data well. It is noted that the data have been uniformly shifted to higher photon energies by 2.4 eV for comparison with the synthetic

spectrum since the atomic kinetics model used here does not include dense plasma line shifts.

The spectral shifts were quantified by the difference between the first moment of the measured He_α line shape and the predicted (unshifted) He_α line shape. The limits of integration were selected to fully encompass the He_α line without contamination from the intercombination line. The uncertainty in the measured shift was calculated assuming independent contributions from dispersion calibration error and statistical signal fluctuations. The measured shift for the spectrum shown in Fig. 150.25(c) was 2.4±0.3 eV.

Figure 150.26(a) shows the measured He_α line shifts for inferred electron densities from 1 to 5×10^{23} cm^{-3}. The dataset is composed of well-resolved spectra with no self-reversal. The error bars are shown for a few representative data points at low, medium, and high densities. The asymmetric vertical error bars reflect the uncertainty in the measured location of the Al K-shell absorption edge used to register the absolute dispersion calibration. This uncertainty does not propagate to the inferred temperature and density since those quantities are sensitive only to the relative dispersion. The data show a nearly linear shift with increasing electron density.[26] The highest electron densities measured were near 80% of solid and were achieved with the high-contrast 2ω drive. The data were selected over a small range of temperatures between 250 and 375 eV.

For each data point, an apparent shift was calculated from the atomic kinetics model to confirm that the observed shifts were not spurious. These data are plotted in red and the typical error is within the data point. The magnitude of the apparent shift appears to decrease with electron density because the 2ω drive for high-density studies produced proportionately higher temperatures that suppress satellite enhancement of the red wings of the line profile.[22]

Predictions from a generalized analytic ion-sphere model proposed by Li *et al.*[19] are compared to the data in Fig. 150.26(a). The analytic approach relies on the self-consistent field ion-sphere model (SCFISM)[27] to obtain the self-consistent density distribution of bound and free electrons within the ion sphere. Relativistic atomic structure calculations of the bound wave functions are carried out in a screened nuclear potential determined from the electron density distribution. Detailed scaling studies were performed to obtain a generalized density- and temperature-dependent formula for the energy level structure in the plasma.

For each data point in Fig. 150.26(a), the analytic formulation was used to predict the line shift at the inferred temperature and density. The calculation is monoenergetic and considers only the $1s2p$–$1s^2$ transition. The calculation agrees well with the data at low density but diverges at higher densities, likely because the calculation neglects unresolved satellites and other contributions to the line shape. An attempt was made to recover this information by adding the apparent shifts to the ion-sphere model predictions. This addition produces better agreement at low and moderate densities, as shown in Fig. 150.26(b). The error bars indicate uncertainty in the calculated shifts based on the density uncertainty in the corresponding data point. The temperature uncertainty was neglected since the model exhibits a weak dependence on electron temperature $\left(\sim T_e^{-0.25}\right)$.

Sensitive spectral measurements of this nature may prove to be a valuable test of electron screening models in extreme conditions. For example, improved agreement between the analytic model and the experimental data is obtained for an *ad hoc* 10% reduction of the ion-sphere radius [Fig. 150.26(b)]. The optimum reduction was determined by a single-parameter maximum-likelihood least squares fit to the data that considered uncertainties in the inferred densities and line shifts. The quality of the match is surprisingly sensitive to the scale factor. It is noted that a 40% increase in the inferred densities can reproduce the improved agreement. It is unlikely, however, that the analysis overestimates the inferred densities by that amount, and it is improbable that densities above solid were achieved in the experiment.

Moreover, spectroscopic temperature and density measurements from K-shell ions can be sensitive to the choice of atomic model. Recent work has demonstrated that model discrepancies can contribute up to 30% uncertainty in the inferred conditions, mostly from uncertainty in Stark-line–shape calculations.[28] Model-dependent temperature and density measurements will become more reliable as theoretical and experimental work further validates line-shape models.

In summary, spectral line shifts of the $1s2p$–$1s^2$ transition in He-like Al ions have been studied as a function of the instantaneous plasma conditions at high energy density. The line shifts were measured using a picosecond time-resolved x-ray spectrometer with an absolutely calibrated spectral dispersion. Buried-layer targets and a high-contrast 2ω laser driver provided access to densities near 80% of solid. The plasma conditions were inferred by comparing the measured spectra to calculations from a NLTE collisional-radiative atomic physics model. A generalized analytic line-shift model was found to be broadly consistent with the experimental data for all but
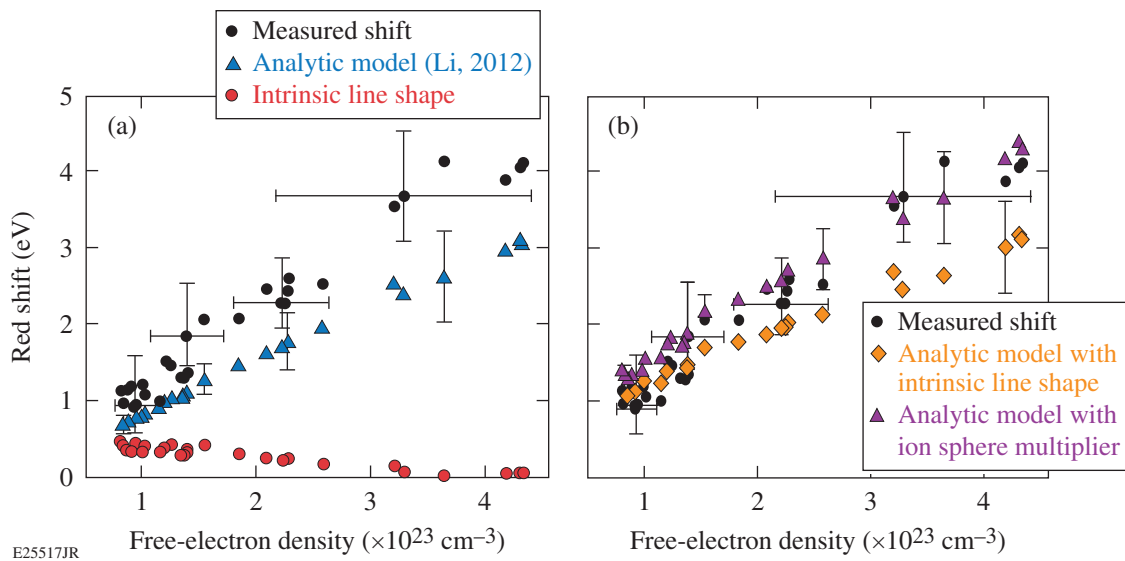

Figure 150.26
(a) Comparison of the data (black) to the analytic line-shift model (blue) and apparent shifts (red). (b) Comparison of the data (black) to the analytic line-shift model plus apparent shifts (orange) and the line-shift model with a scaled ion-sphere radius (purple). The optimum scale factor was determined by a single-parameter least squares fit to the data.

the highest densities studied. These findings are important to understanding plasma-dependent atomic structure and radiation transport in high-energy-density environments.

REFERENCES

1. D. Salzmann, *Atomic Physics in Hot Plasmas*, International Series of Monographs on Physics, Vol. 97 (Oxford University Press, New York, 1998), Chap. 5, pp. 122–146.

2. H. R. Griem, *Principles of Plasma Spectroscopy* (Cambridge University, Cambridge, England, 1997).

3. F. J. Rogers and C. A. Iglesias, Science **263**, 50 (1994).

4. S. Atzeni and J. Meyer-ter-Vehn, *The Physics of Inertial Fusion: Beam Plasma Interaction, Hydrodynamics, Hot Dense Matter*, International Series of Monographs on Physics (Clarendon, Oxford, 2004).

5. O. Ciricosta *et al.*, Nat. Commun. **7**, 11713 (2016).

6. J. Halenka *et al.*, Astrophys. J. **808**, 131 (2015); H. M. Van Horn and V. Weidemann, eds. *White Dwarfs and Variable Degenerate Stars* (University of Rochester, Rochester, NY, 1979), IAU Colloquium 53.

7. D. B. Boercker and C. A. Iglesias, Phys. Rev. A **30**, 2771 (1984); C. F. Hooper, G. C. Junkel, M. A. Gunderson, D. A. Haynes, R. C. Mancini, D. Bradley, J. Delettrez, and P. Jaanimagi, in *Strongly Coupled Coulomb Systems*, edited by G. J. Kalman, J. M. Rommel, and K. Blagoev (Springer US, Boston, MA, 2002), pp. 385–389; G. C. Junkel *et. al.*, Phys. Rev. E **62**, 5584 (2000); H. R. Griem, M. Blaha, and P. C. Kepple, Phys. Rev. A **41**, 5600 (1990).

8. A. Saemann *et al.*, Phys. Rev. Lett. **82**, 4843 (1999); K. Eidmann *et al.*, J. Quant. Spectrosc. Radiat. Transf. **65**, 173 (2000); O. Renner *et al.*, J. Quant. Spectrosc. Radiat. Transf. **99**, 523 (2006); F. Y. Khattak *et al.*, J. Phys.: Conf. Ser. **397**, 012020 (2012).

9. G. Buck, Nature **395**, 51 (1998).

10. X. Li and F. B. Rosmej, Europhys. Lett. **99**, 33001 (2012).

11. V. Bagnoud, I. A. Begishev, M. J. Guardalben, J. Puth, and J. D. Zuegel, Opt. Lett. **30**, 1843 (2005).

12. T. S. Perry *et al.*, Phys. Rev. Lett. **67**, 3784 (1991).

13. C. R. D. Brown *et al.*, Phys. Rev. Lett. **106**, 185003 (2011).

14. C. Dorrer, A. Consentino, D. Irwin, J. Qiao, and J. D. Zuegel, J. Opt. A: Pure Appl. Opt. **17**, 094007 (2015).

15. I. A. Begishev, C. R. Stillman, S. T. Ivancic, S.-W. Bahk, R. Cuffney, C. Mileham, P. M. Nilson, D. H. Froula, J. D. Zuegel, and J. Bromage, "Efficient Second-Harmonic Generation of Large-Aperture Multi-Terawatt Hybrid Nd:Laser Subpicosecond Pulses for Laser–Matter Interactions," to be submitted to Applied Physics.

16. P. M. Nilson, J. R. Davies, W. Theobald, P. A. Jaanimagi, C. Mileham, R. K. Jungquist, C. Stoeckl, I. A. Begishev, A. A. Solodov, J. F. Myatt, J. D. Zuegel, T. C. Sangster, R. Betti, and D. D. Meyerhofer, Phys. Rev. Lett. **108**, 085002 (2012).

17. S. P. Regan, J. A. Delettrez, R. Epstein, P. A. Jaanimagi, B. Yaakobi, V. A. Smalyuk, F. J. Marshall, D. D. Meyerhofer, W. Seka, D. A. Haynes, Jr., I. E. Golovkin, and C. F. Hooper, Jr., Phys. Plasmas **9**, 1357 (2002).

18. J. M. Bañón and H. Nguyen, J. Phys. B: At. Mol. Phys. **20**, 2989 (1987).

19. K. Eidmann *et al.*, J. Quant. Spectrosc. Radiat. Transf. **81**, 133 (2003); P. Hakel *et al.*, High Energy Density Phys. **5**, 35 (2009).

20. U. Andiel *et al.*, Europhys. Lett. **60**, 861 (2002).

21. J. J. MacFarlane *et al.*, High Energy Density Phys. **3**, 181 (2007).

22. A. H. Gabriel and T. M. Paget, J. Phys. B: At. Mol. Phys. **5**, 673 (1972).

23. R. Shepherd *et al.*, J. Quant. Spectrosc. Radiat. Transf. **81**, 431 (2003).

24. J. J. MacFarlane *et al.*, Proc. SPIE **5751**, 588 (2005).

25. F. B. Rosmej, in *Handbook for Highly Charged Ion Spectroscopic Research*, edited by Y. Zou and R. Hutton (CRC, Boca Raton, FL, 2012), Part II, Chap. 12, pp. 267–342.

26. R. Cauble, J. Quant. Spectrosc. Radiat. Transf. **28**, 41 (1982); S. Skupsky, Phys. Rev. A **21**, 1316 (1980).

27. F. J. Rogers, H. C. Graboske, and D. J. Harwood, Phys. Rev. A **1**, 1577 (1970); S. Ichimaru, Rev. Mod. Phys. **54**, 1017 (1982); X. Li, Z. Xu, and F. B. Rosmej, J. Phys. B: At. Mol. Opt. Phys. **39**, 3373 (2006); X. Li and F. B. Rosmej, Phys. Rev. A **82**, 022503 (2010).

28. T. Nagayama *et al.*, High Energy Density Phys. **20**, 17 (2016).